Universität Leipzig

Bachelor Thesis

International Physics Studies Program

Polarimetric Radar Measurements to Analyze the Effect of Aerosol Concentrations on Clouds and Precipitation in Model Simulations with High Resolution

Student
Lucas Eichhorn

Supervisors
Prof. Dr. Klaus Kroy
Prof. Dr. Johannes Quaas

November 2018

Abstract

In the context of climate change, anthropogenic forcings are highly relevant. The target of this study is to better understand how high human-made aerosols affect clouds and precipitation. The hypothesis that cloud condensation nuclei concentrations have an effect on the weather will be confirmed or falsified, and attributed to anthropogenic influence, if possible. To this end, two ICON model simulations were compared, where the aerosol values were changed by a factor of four. The simulation runs were compared to observations. Different, partially polarimetric radar variables were compared, by use of the radar forward model operator CR-SIM. Significant differences were detected in differential reflectivity. No significant differences were detected in specific differential phase. The comparison of simulation with observation does not allow conclusions with regard to the examined hypothesis, because of poor comparability. The results lead to the conclusion that aerosol concentrations affect the weather. To be able to attribute aerosol effects to anthropogenic influence, a valid comparison of simulation data with observation is necessary.

Contents

1 Introduction

Climate change has been subject to research since the 19th century and more extensively since the 20th century. It describes the change in statistical distribution of weather patterns if that change lasts for a longer period of time. It exists a growing body of evidence that climate change is factual, ranging from direct evidence such as the rise in Earth's surface temperature over the last century to indirect evidence such as the sea level change, ice cores and vegetation. As indicators have become more apparent and results of research more clear, the topic has grown to ever more importance.

Climate model projections of the global surface temperature predict an increase from 0.3 °C to 4.8 °C (IPCC [2013]) in the 21st century. Of numerous effects, they include changes in precipitation, the expansion of deserts in the subtropics and the retreat of glaciers. Because of a certain inertia of the climate system, the effects might persist for centuries.

Scientists work to further understand climate (change) through climate records, measurements of observations and through climate models.

Factors that can influence the climate are called "climate forcings" and can be internal or external. Some external natural climate forcings and causes for climate change are the variability of solar radiation, continental drift or the variability of ocean reflectivtiy. Besides deforestation and livestock farming, anthropogenic (external) climate forcings include principally the increase of greenhouse gases, such as carbon dioxide, and the increase of atmospheric aerosols (Wikipedia [2018b]).

Aerosol is particulate matter, fine liquid or solid particles smaller than 1 μm, suspended in the air. It can be everything from smoke, ash, dust, air pollutants over to sea salt and pollen. Aerosols have an atmospheric lifetime of weeks to a few years (Wikipedia [2018g]), being much shorter compared to the lifetime of carbon dioxide. The effects of aerosols on the climate are very complex and still source of great uncertainty in research (IPCC [2001a]). Its direct effects may be both warming of the surface because of solar energy absorption as well as cooling of the surface (Wikipedia [2018a]) because of "global dimming" which entails the reduction of solar radiation reaching the surface. The indirect effect of aerosol on Earth's energy household is the influence on objects that interact with radiation. An increase of cloud condensation nuclei (CCN) for example causes cloud droplets to be smaller and more numerous. CCN also affect precipitation (Khain et al. [2007]), and the lifetime and amount of clouds (Lohmann and Feichter [1997]).

This study examined the effect of CCN on clouds and precipitation, which are still source of uncertainty in climate processes because of the difficulty and complexity of its underlying processes (IPCC [2001b]).

2 Context, Objective and Background

2.1 Practical Context and Objective

The method "detection and attribution" was applied for the examination of the effect of aerosol concentrations. In the context of climate change, detection and attribution describes the statistically valid detection of a change in the climate and the attribution to a cause of that change. To fully confidently determine the cause of a climate effect, experiments in conditions of reality would be necessary. With regard to the impossibility of this undertaking, climate models become useful. For the attribution of a climate effect to a cause, three steps are necessary (IPCC [2007]): a) detection of a climate effect, b) demonstration of its consistency with climate models and c) demonstration of its inconsistency with alternative possible reasons. To this end, climate model simulations are used. The suspected anthropogenic forcings are implemented, isolating its effects by comparison of model runs that differ in a single key factor only.

The present work greatly involved simulations of a climate model. Climate models have become of use to scientists in understanding the climate and its influences, weather forecasting and predictions of climate change since the advent of computational resources in the mid-20th century and its significant advances since then. The models are a representation of reality, forcibly simplify-

ing it because of constraints in both understanding and computational resources. It is still of priority to improve and develop climate models further. Model simulations are tested on past and contemporary observational data.

The ICOsahedral Non-hydrostatic atmosphere (ICON) model was made use of. It is a joint project of the German Weather Service (DWD) and the Max Planck Institute for Meteorology (MPI-M) from 2013. It aims at a unified modelling system for global numerical weather prediction (NWP) and climate modelling (Zängl et al. [2015]).

In this study, the effects of CCN concentrations on the weather were examined by comparing two simulations from the ICON atmospheric model where the CCN value was changed in one of the simulations. In the first run, estimated CCN values from 2013 were used, while in the second one its fourfold value was implemented, simulating the higher anthropogenic aerosol concentration from 1985. The simulation of a specific day in 2013 was chosen to allow the subsequent comparison with observational data from the High Definition Clouds and Precipitation for advancing Climate Prediction (HD(CP)^2) Observational Prototype Experiment (HOPE) project.

The HOPE campain provides weather data measurements of a $10 \times 10 \times 10\,\mathrm{km}^3$ cube near Jülich (50.92 °N, 6.36 °E), Germany (Macke et al. [2017]). Field-experiment measurements were made for the time frame of April and May 2013. The instrumentation included but was not limited to several (and different types of) lidars, radars and radiometers.

To allow for a comparison of radar data between both the atmospheric model simulations and between model simulations and observations, a radar forward operator was used. The Cloud resolving model Radar SIMulator (CR-SIM) takes high resolution Weather Research and Forecasting Model (WRF) data and, according to a set of parameters, produces forward modeled scanning or vertical-pointing radar observation data (Tatarevic and Kollias [2017]). The pulsed doppler K_a-band millimeter radar "MIRA-35" (Wikipedia [2018f]), as used in the above mentioned HOPE project, was taken as reference for the input parameters (Macke et al. [2017]).

In the first comparison of two model simulations, the radar was simulated in scanning mode with an elevation angle of 30 °. Polarimetric radar variables were compared, i.e., radar data produced from both vertically and horizontally aligned electromagnetic waves.

In the second comparison of simulation with observation the radar was simulated as vertically-pointing (elevation angle of 90 °), as observation data is available for a vertically-pointing cloud radar at the site "Krauthausen", near Jülich. Ordinary radar variables were compared, i.e., radar data produced from horizontally polarized electromagnetic waves.

The target of this study is, via the above mentioned method of detection and attribution, to possibly detect an effect on the weather and subsequently attribute it to cloud condensation nuclei. If the change in CCN in the first comparison is found to be substantial, the effect is detected and simultaneously attributed to CCN. Because human-made aerosol emissions were higher in 1985, the comparison with observation data may indicate whether anthropogenic influence was responsible for the effect, depending on which simulation is closer to the measurements.

2.2 Radar Variables

A weather radar is a type of radar that is used to detect and classify precipitation. It emits pulses of horizontally polarized (single-polarization) or both horizontally and vertically polarized (dual-polarization) electromagnetic waves. For Rayleigh scattering (elastic scattering of electromagnetic waves off of particles) to be possible – and therefore for objects to be detected –, the emitted wave must have a wavelength much greater than the encountered object. Between two emitted pulses of the order of 1 microsecond, the radar waits for 1 millisecond for reflected signals (return echos) that are caused by the reflection of the signal by the encountered object. Depending on object shape, size, refractive index and number concentration, wave properties are changed and thus give information about the detected objects.

Single-polarization radars measure the radar variables reflectivity, radial/Doppler velocity and spectrum width. Dual-polarization radars also measure differential reflectivity, differential prop-

agation phase shift, specific differential phase, linear depolarization ratio, and the co-polar correlation coefficient. Dual-polarization radars allow for richer information and more possibilities of comparison (cf. section 5). The polarimetric radar variables relevant for the first comparison (section 4.1) differential reflectivity Z_{DR} and specific differential phase K_{DP}, as well as the conventional radar variables, horizontal reflectivity Z_{h}, radial/Doppler velocity V_D and spectrum width SW will be introduced.

2.2.1 Horizontal Reflectivity $Z_{\mathbf{h}}$

It is a measure of the radiation fraction reflected by the target, or how efficiently it returns the energy received by the horizontally polarized electromagnetic wave. Reflectivity depends on the sixth power of the target's diameter D and the drop size distribution $n(D)$ which depends on the diameter:

$$Z = \int n(D) D^6 dD$$

It therefore gives information about the size (or here specifically its horizontal extent) of the target and its number concentration which may, for instance, translate to precipitation rate. It is either measured in $\mathrm{mm}^6\,\mathrm{m}^{-3}$ (reflectivity factor) or, as done here, on a logarithmic scale in the dimensionless unit of dBZ:

$$\mathrm{dBZ} \sim 10 \log_{10} \frac{Z}{Z_0}$$

where Z_0 is the equivalent reflectivity return of a 1 mm drop in a volume of one meter cube. 0 dBZ represents a hardly noticeable intensity of rain, 25 dBZ light, and 50 dBZ heavy rain.

2.2.2 Radial/Doppler Velocity V_D

By use of the Doppler Effect, the radial velocity component is obtained, or, the velocity component along the radar beam. The positive axis is usually defined away from the radar (outbound). The quantity represents a mean taken of all target radial velocities present in the radar sampling volume. It has the unit m/s.

2.2.3 Spectrum Width SW

It is a measure of the velocity dispersion of the radar sampling volume. I.e. the variability of mean radial velocities of the scattering objects. As explained in section 3.2.1, it has different contributions, such as velocity dispersion due to wind shear or turbulence. It has the unit m/s. Values range from 0 m/s to usually 10 m/s where low values represent smooth flow and high values turbulent, chaotic flow.

2.2.4 Differential Reflectivity Z_{DR}

It is the logarithmic ratio of horizontal and vertical reflectivity factors and a measure of the (reflectivity-weighted) axis-ratio, i.e. the shape of the target. It is measured in dB and is independent of number concentration.

$$Z_{DR} = 10 \log_{10} \frac{Z_h}{Z_v}$$

This means, horizontally aligned particles return positive values, vertically aligned ones negative values and circular shaped objects (or statistically circular shaped objects such as tumbling hail) return 0 dB. For meteorological objects, values range from -1 to 6 dB (Kumjian [2013]) where it is noted that atmospheric water drops increase their relative horizontal extent with increasing size.

2.2.5 Specific Differential Phase K_{DP}

A horizontally and vertically polarized electromagnetic wave that is emitted by the radar acquires a phase shift due to the propagation through a medium. The acquired phase shift is usually higher when the wave traveles through a different medium than air and according to the shape of the target, it can be different horizontally to vertically. The specific differential phase describes the difference in phase shift acquired per unit distance along the radar beam. It is expressed in °/km and is proportional to number concentration and particle size. The values range from $-1\,°$/km (for vertically oriented ice crystals) to $+10\,°$/km (for hail and graupel, Kumjian [2013]).

3 Methods

For the comparison of the two model runs with different CCN values, data of the ICON simulation model was used. Its output was converted to

radar data using the forward model operator CR-SIM. From that the two dimensional plots were created.

3.1 ICON Modelling Framework

The ICOsahedral Non-hydrostatic atmosphere model produces high-resolution simulation data. For the purposes of the present study, ICON was applied in the Large-Eddy Simulations (LES) configuration (Heinze et al. [2017]). Its main purpose is a better understanding of cloud and precipitation processes, the development of parametrization of moist diabatic processes for general circulation models (GCM) and the assessment of rapid responses of clouds to anthropogenic forcings in perturbed simulations.

ICON simulations were evaluated and compared with the COnsortium for Small-scale MOdelling (COSMO) model and with observational datasets obtained from the HOPE project. They possess a horizontal resolution of 156 m that is beneficial to the representation of processes at subgrid-scale for regular models. In the above-mentioned study of 2016 that has been used for the present study, four days in spring 2013 have been simulated. For evaluational purposes, the days were chosen in such a way as to match observational data from the HOPE project.

ICON has three physics packages: one for Numerical Weather Prediction (NWP), one for climate modelling and one for LES. In the above mentioned study, a real case configuration was used, with lateral boundary conditions and a one-way nesting approach.

The model configuration solves the variables suggested by Gassmann and Herzog [2008] including the horizontal velocity component normal to the triangle edge, the velocity component tangential to the triangle edge, the vertical velocity component, the density of moist air, the virtual potential temperature, the mass fractions, and number densities of a number of tracers, including the mass fraction of water vapor and different hydrometeors (Heinze et al. [2017]). The horizontal discretization is done by triangular cells which in total form a icosahedron. A C-type stagger is used, where the normal velocity component is defined at triangle edge midpoints, and where all other variables are defined at cell circumcentres. The vertical discretization is done with a height-based terrain-following coordinate system and it uses a Lorenz-type staggering where the vertical velocity is defined at interface/half levels and the other variables at main/full levels. The microphysical parametrization (scheme of Seifert and Beheng [2006]) predicts the mass fractions and number densities of cloud droplets, rain, cloud ice, snow, graupel and hail. The configuration of the cloud condensation nuclei is based on a simulation of the aerosol conditions of the COSMO Multi-Scale Chemistry Aerosol Transport model (Wolke et al. [2004, 2012]) where the profile was chosen such as to represent typical conditions for the simulated days. Until 1500 m altitude the CCN concentration remains constant, and above it decreases.

ICON uses different time steps. The applied fast and slow-physics routines are called on every time step or every specified multiple time step, respectively. The simulation set-up is such that it corresponds to the observational data obtained in the HOPE project. The latter covers an area of $10 \times 10\,\mathrm{km}^2$ near Jülich in the very west of Germany.

The model top is at 21 km altitude and it has 150 vertical levels with varying thickness. It has three refined domains ("nests"), and their resolution is halved from 625 m, to 312 m, to 156 m at the innermost domain at each grid refinement step. Correspondingly, the fast physics time-step is also halved at each refinement step, from 3 s at the coarsest domain to 0.75 s at the inner domain. The slow-physics time-step is 900 s for all domains.

For the evaluation of the ICON model, other simulations have been consulted (Heinze et al. [2017]). Namely the COSMO model and two conventional LES models: the PArallelized Large eddy simulation Model (PALM) and the Dutch Atmospheric Large-Eddy Simulation model (DALES). For further evaluations of non-conventional observations, a range of forward operators have been used: the visible satellite forward operator (VISOP) that generates radiances for the solar channels of the Moderate Resolution Imaging Spectroradiometer satellite instrument, the Synthetic Satellite imagery (SynSat) that generates infrared satellite data, the Passive and Active Microwave radiative Transfer RAdar

simulator (PAMTRA) that enables comparison with cloud radar data, and the Efficient Modular Volume RADar Operator (EMVORADO) that enables comparison with 3D scan measurements from BoXPol and the C-band radar network of the German Weather Service.

The simulation output for 3D snapshots, used for the comparisons of this study, occurs at a frequency of 1 hour. Datasets exist from 06:00 UTC to midnight. Originally the output is produced on each of the three domains on the triangular grid. For purposes of the abovementioned study, however, it has been converted to a regular geographic (lat/lon) grid.

Each day of simulation produces 50 TB of data that is being post-processed and distributed to its various users, according to individual requirements, via a workflow team.

Four days in April and May 2013 close to the city Jülich in the west of Germany have been simulated as they reflect a range of different weather conditions from high-pressure calm and clear-sky weather to deep clouds and precipitation.

Overall, model evaluations show that the ICON model in LES configuration is in most aspects of weather prediction as comparably good as the established COSMO model. Some shortcomings include: small shallow cumulus clouds are produced too large, biases in the thermodynamic profiles, surface temperatures are too low over extended areas, and precipitation particles are too large.

3.2 CR-SIM Radar Forward Operator

In the context of the forward or inverse problem (Wikipedia [2018d]), with the following equation

$$d = G(m)$$

where d is observed data, m model data and G an operator describing the explicit relationship between observed data and model parameters, CR-SIM represents G. It is a radar forward model operator that converts weather simulation model data into radar data. This enables direct comparison between the model output and observational radar data.

The operator is able to work with several double-moment microphysics schemes (such as the Thompson et al. [2008] or Morrison et al. [2005, 2009] scheme) and the bin explicit scheme. Only the ICON model with Seifert and Beheng [2006] double moment microphysics scheme will be considered here as it is the relevant one for the present study.

3.2.1 Input and Output

As input, CR-SIM uses the ICON model output, whose format has to be consistent with the Weather Research and Forecasting Model (WRF) microphysics format. The produced output takes the form of one main file, with total hydrometeor content, and six additional files, one for each hydrometeor category (cloud, rain, ice, snow, graupel, hail) respectively (Tatarevic and Kollias [2017]).

Depending on the parameters entered in the User Parameter File (see section 3.2.3), the files comprise different output variables. The "radID" parameter controls whether polarimetric variables are computed and the "ceiloID" parameter controls whether the simulations of ceilometer measurements are included. In this study it was not made use of the latter.

The variables computed by CR-SIM are (Tatarevic and Kollias [2017]):

- Radar reflectivity factor at horizontal polarization $\boldsymbol{Z_h}$ [$\mathrm{mm^6/m^3}$ or dBZ]
- Radar reflectivity factor at vertical polarization $\boldsymbol{Z_v}$ [$\mathrm{mm^6/m^3}$ or dBZ]
- Co-polarization radar reflectivity factor $\boldsymbol{Z_{vh}}$ [$\mathrm{mm^6/m^3}$ or dBZ]
- Differential reflectivity $\boldsymbol{Z_{DR}}$ [unitless or dB], defined as the ratio between the fractions of horizontally polarized backscattering and vertically polarized backscattering
- Linear depolarization ratio $\boldsymbol{LDR_h}$ [unitless or dB], defined as the ratio of the power backscattered at vertical polarization to the power backscattered at horizontal polarization for a horizontally polarized field
- Specific differential phase $\boldsymbol{K_{DP}}$ [°/km], comparison of the backward phase difference between the horizontally and vertically polarized waves
- Differential backscatter phase $\boldsymbol{\delta}$ [°], defined as the difference between the phases of horizontally and vertical polarized components

of the wave caused by backscattering from the objects within the radar resolution volume
- Specific attenuation at horizontal polarization $\boldsymbol{A_h}$ [dB/km], or for horizontally polarized waves, represented by forward scattering amplitudes
- Specific attenuation at vertical polarization $\boldsymbol{A_v}$ [dB/km], or for vertically polarized waves, represented by forward scattering amplitudes
- Specific differential attenuation $\boldsymbol{A_{DP}}$ [dB/km] is defined as the difference between the specific attenuations for horizontally and vertically polarized waves
- Mean Radial Doppler velocity $\boldsymbol{V_D}$ [m/s], positive away from the radar (radar notation)
- Mean Vertical Doppler velocity $\boldsymbol{V_{D_{90}}}$ [m/s], positive upward (radar notation)
- Spectrum width SW_{TOTAL}. There are six major spectral broadening mechanisms that contribute to the spectrum width SW_{TOTAL} measurements (Doviak and Zrnic [2006]):

  1. different hydrometeor terminal velocity of different sizes SW_H
  2. turbulence SW_T
  3. mean wind shear contribution SW_S
  4. cross wind contribution SW_V
  5. antenna motion SW_A
  6. contributions due to variation of orientation and vibrations of hydrometeor SW_O

  Therefore the total spectrum width is:

$$SW_{TOTAL} =$$
$$({SW_H}^2 + {SW_T}^2 + {SW_S}^2 +$$
$${SW_V}^2 + {SW_A}^2 + {SW_O}^2)^{0.5}$$

  However, contributions SW_A and SW_O are not estimated here and their contributions to SW_{TOTAL} are considered negligible compared to contributions of other terms. Computed and outputted contributions however include SW_H, SW_T, SW_S and SW_V, and the total spectrum width SW_{tot} is calculated as

$$\boldsymbol{SW_{tot}} = \sqrt{{SW_H}^2 + {SW_T}^2 + {SW_S}^2 + {SW_V}^2}$$

- $\boldsymbol{SW_{H_{90}}}$, representing the spectrum width due to different hydrometeor terminal velocity of different sizes in vertical, such that $SW_{H_{90}} = SW_H(\theta = 90\,^\circ)$
- Reflectivity weighted velocity $\boldsymbol{V_{RW}}$ [m/s], (positive downward)
- radar sensitivity limitation with range Z_{MIN} [dBZ], computed as follows:

$$\boldsymbol{Z_{min}}\,[\text{dBZ}] = Z_0\,[\text{dBZ}] + 20\,\log_{10}(r\,[\text{km}])$$

  where $\boldsymbol{Z_0}$ is configurable term defined in the User Parameter File, while r is the radar range in km

For the operation of CR-SIM and the computation of radar variables, it is made use of look-up tables (LUT). They contain pre-computed complex scattering amplitudes of electromagnetic waves, emitted by hydrometeors upon incidence of the incoming radar pulse signal wave. The scattering process depends on the direction of incidence and scattering of the electromagnetic wave as well as on the size, shape and composition of the particle. The mathematical relation between the incident and the scattered field is assumed by a scattering matrix. It is calculated using Mishchenko's T-matrix code of a non-spherical particle at a fixed orientation. The required variables for the T-matrix code such as axis ratio, radar wavelength, elevation angle, particle orientation and width of canting angle distribution[1] are specified in the User Parameter File. This way, the correct LUT needed during the operation can be determined. For the computation of the LUTs, all particles are modeled as dielectrically dry, oblate spheroids.

3.2.2 Operation

The operation algorithm of CR-SIM works as follows: First the User Parameter File is read. Then the input dataset, formatted according to WRF, is read, the needed meteorological variables are reconstructed[2] and the enquired domain extracted. For each grid point of the domain and

[1] where the mean canting angle is assumed to be zero degrees for all hydrometeors
[2] the meteorological variables reconstruced are pressure, temperature and height

each hydrometeor type the nearest look-up table is determined. The LUT is read, radar variables are computed and the necessary data for the computation of the "total hydrometeor content" is saved. After going through each hydrometeor type, the radar variables for the total hydrometeor content are calculated and computation is finalized. Last the files are written out in NetCDF format.

3.2.3 Parameters

The following parameters have been used (where the two values in "elevation" refer to the first and second comparison, section 4.1 and section 4.2, respectively):

height of radar, above sea level	99 m
radar position	centered
radar frequency	35 GHz
elevation	30 °/ 90 °
radar beam width	0.5 °
radar range resolution dr	30 m
coefficient Z_0	−55 dBZ

Table 1: Radar parameters

The scattering types (mathematical parametrization of hydrometeors) that have been assigned to respective hydrometeors are:

Hydrometeor	Scattering Type[3]
cloud	*cloud*
rain	*rainb*
ice	*ice_ar0.20*
snow	*snow_ar0.60*
graupel	*graupel_ar0.80*
hail	*gh_ryzh*

Table 2: Applied scattering types

It has been used the same threshold of mixing ratio of $1 \times 10^{-8}\,\mathrm{kg\,kg^{-1}}$ for all hydrometeor classes.

The orientation distribution for all hydrometeors is the 2D Gaussian model with zero mean and sigma standard deviation where sigma is 10 ° for cloud, rain, ice, and 40 ° for snow, graupel, hail.

[3]Tatarevic and Kollias [2017]

3.3 Creation of Diagrams, Use and Treatment of Data

For the first comparison (section 4.1), the raw ICON model output was averaged out from a temporal resolution of 15 min to 1 h. Afterwards, simulated radar data was computed by the forward model operator CR-SIM. For that a certain format is required in which the data firstly had to be converted into. This was done by reading in the data with python (using the NumPy library), extracting the values and inserting them into a dataset with the set up dimensions and variables. The forward operator's output consists of one main output file with total hydrometeor content, and six other files for the hydrometeor categories cloud, rain, ice, snow, graupel and hail (cf. section 3.2). For the purposes of this study, only the total hydrometeor content datasets have been used. For the first comparison, forward operated data was averaged out over the time frame of 6 hours (cf. section 4.1). From the radar data, the plots were created, again using python (with NumPy and matplotlib libraries). For the second comparison, radar data was averaged out with python (cf. section 4.2) and then plotted.

4 Results

In this section the results will be presented. First, the comparison of the two ICON model simulations, and second the comparison of the simulational and the observational data. In Fig. 1 and Fig. 2, the y-axis is not to scale as height levels vary in thickness. The height has been clipped at 9 km, little below tropopause level. Height level values have been rounded to 10 m. The simulation data used has been forward operated by the radar forward operator CR-SIM (cf. section 3.2).

4.1 Comparison of Simulations, 1xCCN and 4xCCN

For the comparison of simulations, data has been restricted to 6 hours from 5/2/2013 18:00 UTC to 5/3/2013 00:00 UTC. CR-SIM was applied with an elevation angle of 30 ° (cf. section 3.2). The comparison of the radar variables is done by vari-

able. First, differential reflectivity Z_{DR}, and second specific differential phase K_{DP} are analyzed. Each variable is compared both averaged over latitudes as well as averaged over longitudes, covering an area of 6.09–6.73 °E, 50.70–51.11 °N, resulting in $46 \times 46\,\mathrm{km}^2$ near Jülich. It was chosen to compare the simulations by one plot showing radar forward operated simulation data where the CCN values from 2013 were plotted (referred to as "1xCCN") and a plot showing the relative difference of the simulations, in order to facilitate the quantification of the relative differences between simulations. The relative difference was computed according to

$$var_{\mathrm{reldiff}} = \frac{1\mathrm{xCCN} - 4\mathrm{xCCN}}{1\mathrm{xCCN}} \qquad (1)$$

where "4xCCN" refers to the simulation with CCN values from 1985, and where the 1xCCN values in the divisor below the absolute value of 0.1 dB for Z_{DR} and below the absolute value of 0.1 °/km for K_{DP} have been masked as to avoid misleading values of relative difference. The values are displayed by contours. For the relative difference, the scale was reajusted, clipping $Z_{DR_{\mathrm{reldiff}}}$ values below −300% and $K_{DP_{\mathrm{reldiff}}}$ values below −167% for better visibility. The colors representing a specific value range are coherent by variable. Masked values appear white.

4.1.1 Differential Reflectivity

The Z_{DR} values (Fig. 1, left) range from 0 to 2 dB and are therefore located at the lower end of the spectrum. In both plots of differential reflectivity, values stay mostly in the range of 0.2 to 1 dB; only partially higher values of up to 1.4 dB (above) or 2 dB (below), respectively, are observed. Some parts have masked values indicating no reflection signal.

The lower Z_{DR} values stem from nonmeteorological object or Bragg scattering. Considering variable implications of object shape, the higher values indicate a slightly horizontally oriented object axis. The classification of likely objects results in small (supercooled) water droplets or ice crystals. Other classifications (hail, graupel, snow) can be excluded due to overall weather conditions. Since the plots represent weather data that has been averaged over 6 hours, precipitation cannot, however, be excluded for short periods of time.

In the plot showing Z_{DR} values averaged over latitudes, there is a region of equably distributed values at heights 3–8 km, with Z_{DR} from 0.2 to 0.6 dB. An area of higher values at heights 4.6–5.8 km is visible in the eastern region, 6.65–6.7 °E, with values from 0.6 to 1.4 dB.

Evaluating pattern and value distribution, equably distributed mid-level cloud types are considered to be possible. The corresponding cloud types are: altostratus, altocumulus, cirrus, cirrocumulus, cirrostratus.

Considering the relative difference plot, relatively small differences from 4xCCN to 1xCCN simulation in the range of −50 to +50% are observed for the most part, with some regions of a relative difference from +50 to +100%. At two strips near the boundary of the cloud, there are greater relative differences observable: a horizontal layer at 5 km, from 6.1 to 6.43 °E, with a relative difference of up to −300+%, and another, greater region at 3 km height, from 6.4 to 6.7 °E. It shows a relative difference of up to −300+%, too, where values of greater negative relative difference (in the lower part), as well as overall negative relative difference values spread over more height levels than the above mentioned strip.

In the second Z_{DR} plot, averaged over longitudes, smaller values in the same heights as in the first are observed, 3–8 km height, being slightly higher at heights from 4.6 to 8 km, with values of up to 1 dB. At 4.7 km height, 51.08 °N, it exists a spot of highest Z_{DR} value of 2 dB. It is of 2 km length and 400 m thickness and represents particles locally with a (relatively) more oblate shape.

Considering both plots simultaneously, averaged over latitudes and averaged over longitudes, it is noted that the spot of 2 dB at 51.08 °N and the region of elevated Z_{DR} values at 6.65 to 6.7 °E probably represent a part of the same object, being located in the north-east of the area.

Evaluating pattern and value distribution, equably distributed mid-level cloud types are considered to be possible, as the evaluation of the plot above did as well. Possible cloud types are: altostratus, cirrus.

Like in the first plot of relative difference, here too, $Z_{DR_{\mathrm{reldiff}}}$ reaches values of ±50%, and some regions of a relative difference from +50 to

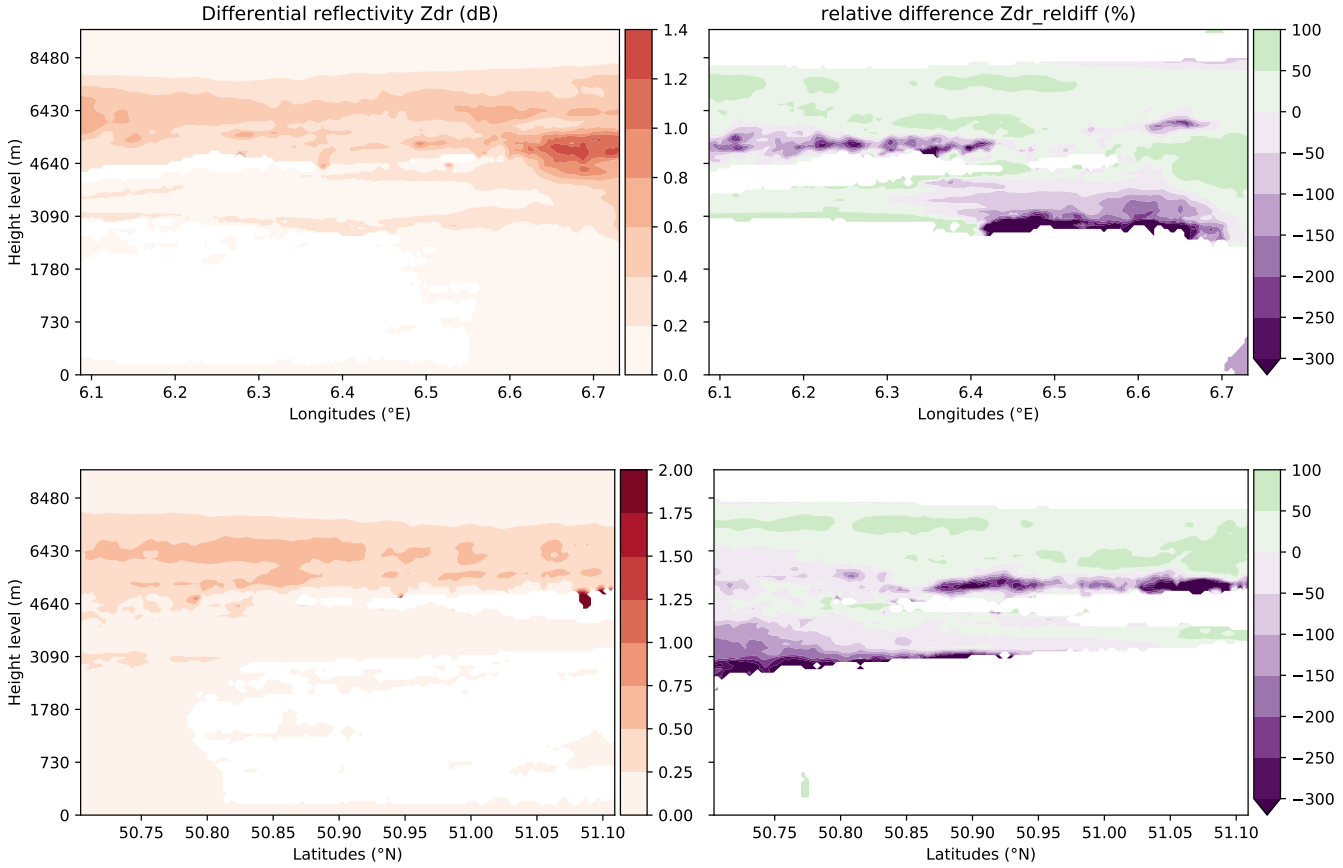

Figure 1: Comparison of simulations, 1xCCN Z_{DR} (left) and $Z_{DR_{\text{reldiff}}}$ (right), averaged over latitudes (above) and averaged over longitudes (below)

+100%. At 5 km height, 50.85–51.1 °N, a horizontal layer from −100 to −300+% values is noted. Furthermore, there is a region at 50.7–50.95 °N, spreading out southwise from 3.1 km heights at 50.95 °N to 2.5–3.9 km heights at 50.7 °N, with relative difference values from −100 to −300+%.

When considering both plots at the same time, averaged over latitudes and averaged over longitudes, one notes a coherent depiction of $Z_{DR_{\text{reldiff}}}$ conditions, i.e. higher 4xCCN Z_{DR} values at lower heights in the south-east and at mid-level in the north-west.

For the most part of the area of the cloud ($\sim 80\%$), the relative difference stays in the range of $\pm 100\%$, i.e. the 4xCCN Z_{DR} values double with respect to their corresponding 1xCCN value or reduce to 0. The remaining part ($\sim 20\%$) of the area has higher relative differences on the negative scale, of up to −300+%. Or, put differently, heights and surface area (latitudes and longitudes) of both $Z_{DR_{\text{reldiff}}}$ plots appear to be equally of negative/positive relative difference (green/violet color distribution). But on negative regions, $Z_{DR_{\text{reldiff}}}$ values reach higher negative values than on positive regions.

Therefore, it can be inferred that 4xCCN Z_{DR} values are higher over more heights and greater surface area than 1xCCN Z_{DR} values. This holds true especially for heights up to 5 km.

This indicates that the particles are more oblate in the 4xCCN simulation than in the 1xCCN simulation. The 4xCCN simulation thus produces bigger (supercooled) water droplets or ice crystals at mid-level, pointing to both before considered mid-level cloud types, altocumulus and altostratus.

4.1.2 Specific Differential Phase

Both K_{DP} plots are very similar, only mirrored vertically. They will be compared simultaneously. For a great part, the values are either masked (indicating no signal) or very small ($\leq 0.15\,°/\text{km}$).

At about the heights 5.6–8.5 km, the values of specific differential phase range from 0.15 to 0.9 °/km and are thus located at the lower end of the spectrum.

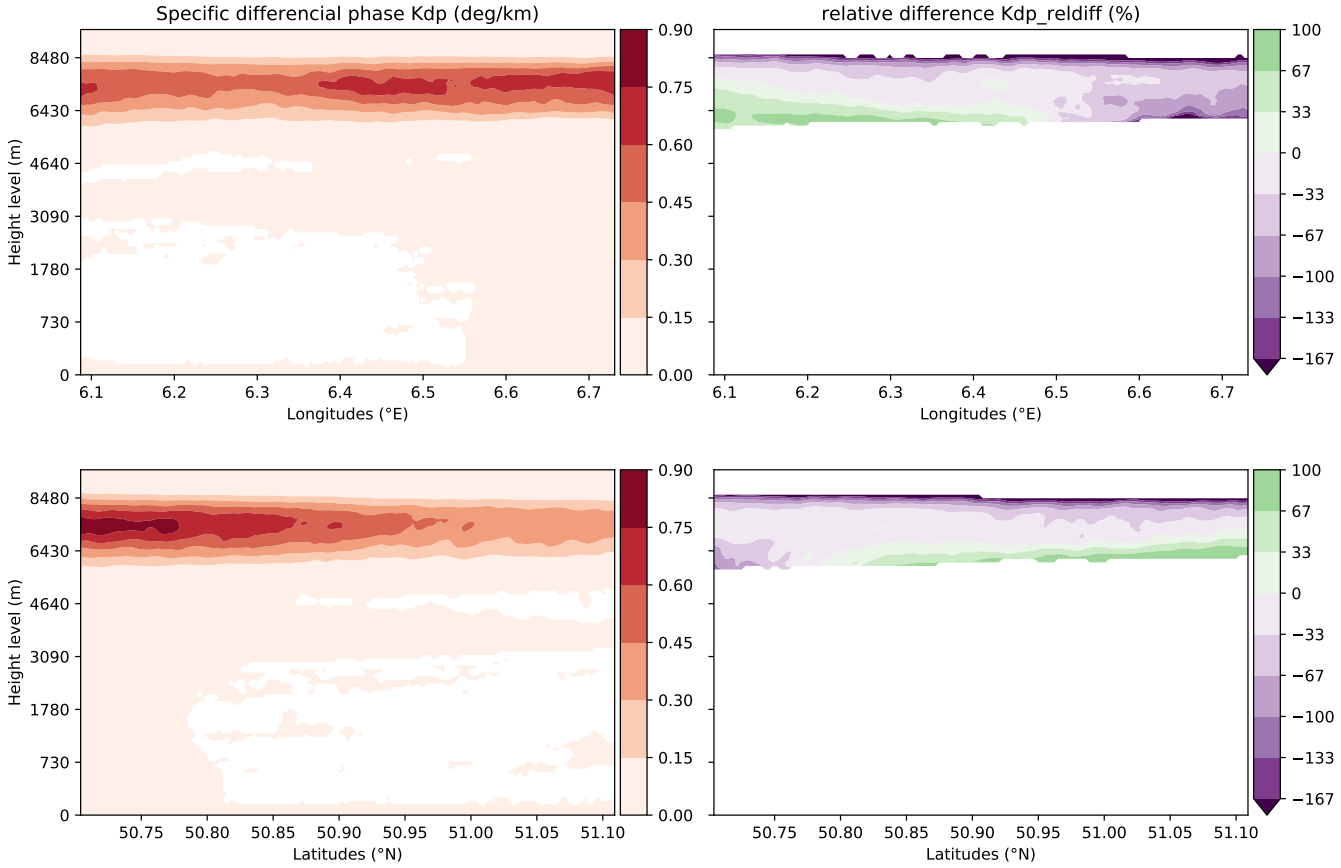

Figure 2: Comparison of simulations, 1xCCN K_{DP} (left) and $K_{DP_{\text{reldiff}}}$ (right), averaged over latitudes (above) and averaged over longitudes (below)

At given height levels, values increase towards the east, reaching 0.6–0.75 °/km at 6.4–6.7 °E, and to the south respectively, reaching 0.75–0.9 °/km at 50.7–50.9 °N. Noting that specific differential phase is affected by number concentration and particle size, the plots are indicating an increasing number concentration towards the south-east, or an increase in particle size.

Taking into account both plots simultaneously, averaged over latitudes and averaged over longitudes, one remarks that the cloud increases its number concentration (or particle size) towards the south-east. The given pattern and value range suggest cloud types of high level, such as cirrostratus and cirrocumulus.

Considering both variables, from a superposition of Z_{DR} and K_{DP} plots, more information about resulting cloud types can be gained. The Z_{DR} plots suggest light mid- to high-level cloud types, with slightly oblate particles. By taking into account the Z_{DR} plot, the higher K_{DP} values indicate a higher number concentration (and not larger sized particles), since differential reflectivity is not affected by number concentration and since larger particles would show in the Z_{DR} plot by being more oblate. This leads to the conclusion of a stratus type cloud at upper height levels (by K_{DP}).

Considering now the relative difference plot (Fig. 2, right), a decreasing gradient is observed from the lower west height (6.1 °E) to the higher east levels (6.7 °E), and from the lower north levels (51.1 °N) to the higher south levels (50.7 °N). Equation (1) implies that the 4xCCN cloud becomes more dense (higher particle concentration) towards the south-east compared to the 1xCCN cloud.

In both averaged plots, the relative difference ranges from −167 to +100% (excluding clipped values). It can be concluded that the 4xCCN cloud has a higher overall particle number density.

This is to be expected, since a higher concentration of CCN physically leads to an increase in the number of cloud droplets. At the same time, particle size decreases. This does not contradict

the evidence from $Z_{DR_{\mathrm{reldiff}}}$ plots, where at corresponding heights[4] lower 4xCCN Z_{DR} values indicate that particles are less oblate and therefore smaller.

In comparison to Z_{DR} plots, here the difference is reasonably smaller. For most of the cloud area ($\sim$ 80%), the relative differences are up to $\pm$67%. The remainder ($\sim$ 20%) has higher relative differences of up to +100% or −167%. The gradient in the relative difference mentioned above gives raise to the suspicion that the same cloud is simulated with a fourfold CCN value, just shifted to the south-east.

4.2 Comparison of Simulation with Observation

For the comparison of the simulation with observation data, the simulational data is presented similarly to the observational one. The radar forward operator CR-SIM was applied to the simulation data with an elevation angle of 90 °. Height levels are shown up to around 12 km. The time frame comprises 5.25 hours from 2/5/2013 18:45 to 3/5/2013 00:00 (UTC). Since the ICON simulation data was available at a resolution of 15 min, a bilinear interpolation method was applied. The data, being averaged over latitudes and longitudes, has been ajusted[5] as to fit the represented area for Krauthausen in the HOPE project: 6.3446 – 6.4844 °E, 50.8347 – 50.9247 °N, covering a surface area of $10 \times 10\,\mathrm{km}^2$. Same colormaps were chosen if available, such as for variables Z_{h} and SW_{tot}. For V_{D} a similar one was chosen. Color levels were ajusted. Masked values in the simulations were filled with values of −60 dBZ for Z_{h} and 0 m/s for V_{D} and SW_{tot} for scale ajustment and better visibility. Interpolation between masked values causes the noise-like pattern in the SW_{tot} plot (Fig. 5).

The simulation presented in the comparison of Fig. 3, 4 and 5 is the 4xCCN run, as it appears to be slightly closer to observation.

4.2.1 Horizontal Reflectivity

Since reflectivity depends on the number of drops per unit volume, and on (the sixth power of) particle diameter (Wikipedia [2018c]), the very low Z_{h} values from −30 to −5 dBZ, that are mostly present in the simulation plot, indicate small droplet sized water or ice particles, or a very low number concentration of particles.

At 18:45 UTC, there is a cloud at heights 6.5–9 km as well as small droplets distributed over 400 m thickness at heights 3.5–4 km. The upper cloud steadily becomes slightly bigger to 3.5 km thickness at midnight, from 5.5 to 9 km, while the lower (second) cloud element remains in its height and thickness, only disappearing from 20:45 to 21:45 UTC. The remaining heights are at values below −30 dBZ, indicating noise or Bragg scattering.

In the observation plot, values tend to be slightly lower, from −30 to −10 dBZ. According to the Tropos website (TROPOS [2018]), displayed values are classified as ice (in higher levels) and drizzle (at around 2 km).

Starting at 19:15 UTC, a cloud starts to form at heights 7–8 km to 6–9 km at 20:15 UTC, while at the height of 2.5 km and below a small area of reflected particles represent drizzle, from 19:30 to 20:15 UTC. The upper cloud becomes bigger until midnight, to a thickness of 4 km, from height levels 5–9 km, where from 22:40 UTC onwards particles at the lower area (5 km) tend to have slightly increased values to a maximum of −10 dBZ.

4.2.2 Radial Velocity

The simulation plot shows radial velocities from 0 to 3 m/s downward. Since the elevation angle is 90 °, the data does not comment on the horizontal velocity component.

At 18:45 UTC, there are downward velocities from 1 to 2.5 m/s at heights of 7 to 10 km. Downward velocities of 1–1.5 m/s are also seen at height levels 3.5–4 km. The velocity distribution at upper heights has a small variation until midnight, extending itself to 3 m/s downward, while the corresponding height levels increase to heights 5.5–9 km. The lower velocity heights remain in its height levels and value, disappearing from 20:45 to 21:45 UTC. All other values are below 1 m/s.

The observation plot shows the same pattern as the observation of horizontal reflectivity

[4] at regions of positive relative difference

[5] supposing hereby that the Krauthausen site lies at the center of the $10 \times 10 \times 10\,\mathrm{km}^3$ cube

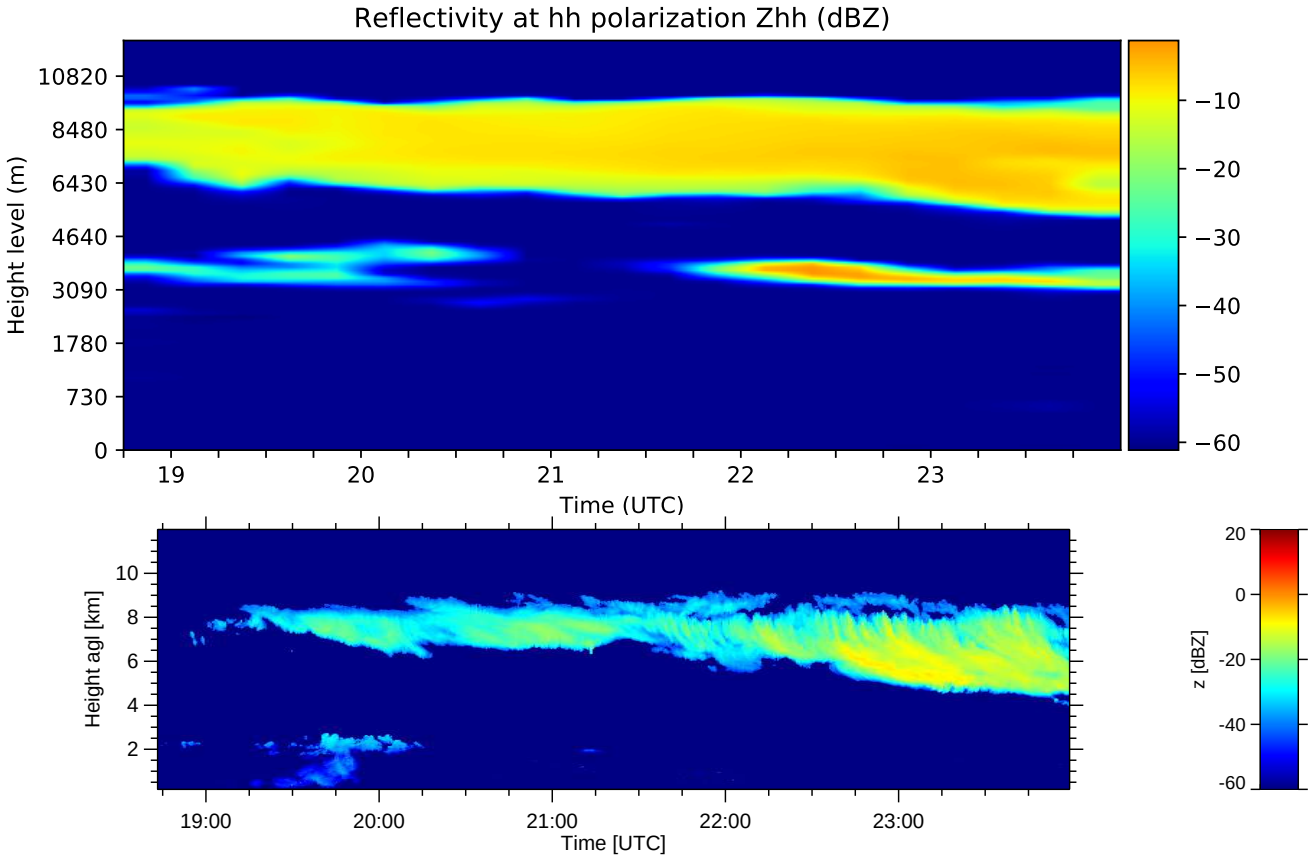

Figure 3: Z_{h} for Krauthausen, above: ICON-Simulation, 4xCCN; below: HOPE-Observation

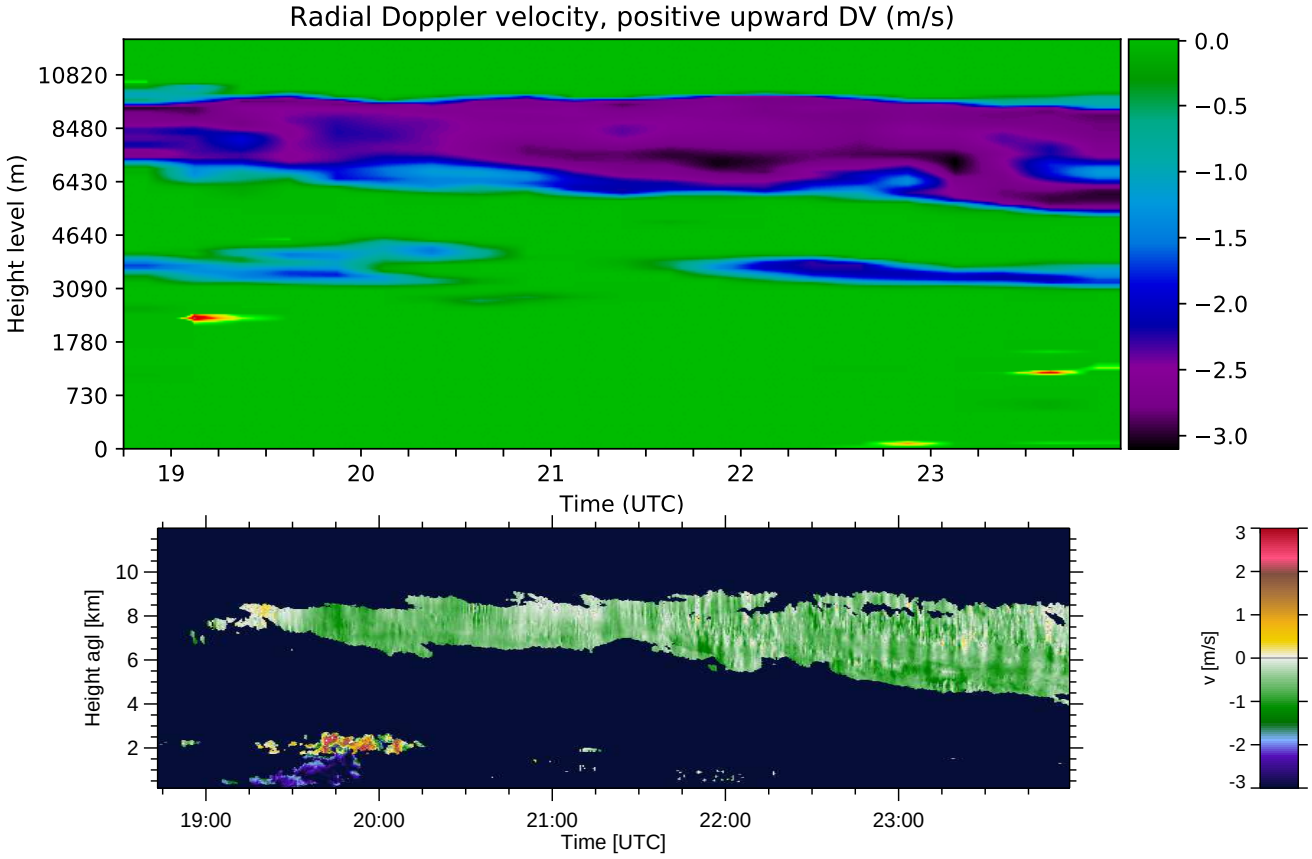

Figure 4: V_{D} for Krauthausen, above: ICON-Simulation, 4xCCN; below: HOPE-Observation

(Fig. 3) with downwards velocities of 0–1.5 m/s in the upper velocity height levels, having upward velocities from 19:10 to 19:20 UTC and punctually afterward, mostly after 23:15 UTC. The lower velocities height levels at around 2 km from 19:15 to 20:15 UTC have velocities from 0 to 3 m/s downward as well as upward.

4.2.3 Total Spectrum Width

In the simulation plot, a total spectrum width is displayed mainly with a range from 0.05 to 2 m/s.

At 18:45 UTC at heights 6.5–10 km the velocity dispersion is mostly from 0.7 to 2 m/s. At the same time, at 3–4 km height levels, there is a total spectrum width of 0.1–0.4 m/s. The upper heights of dispersion decrease slightly in range to 0.5–1.5 m/s, increasing in height levels to 5–10 km up to midnight. The lower heights of dispersion increase in thickness to 1.5 km (3–4.5 km heights) from 19:15 to 20:45 UTC. After virtually disappearing at 20:45 UTC, they reappear in 1 km thickness 21:30 UTC. All other values are at around 0.01 m/s.

The observation plot (Fig. 5, below) shows again the same pattern as the other observational plots (Fig. 4, below and Fig. 3, below). Total spectrum width values in said heights range from 0.08 to 3 m/s. The lower heights of dispersion show values mostly near 3 m/s, from 19:15 to 20:15 UTC. The upper heights mostly range from 0.1 to 1 m/s total spectrum width, with increased values at 19:00–19:30 UTC, 20:45–21:15 UTC, and in upper height levels from 21:20 UTC onward in phases of up to 5 minutes.

Evaluating the three simulation plots and corresponding observation data, it is clear that the comparability is limited due to comparably low temporal resolution of ICON data of 15 min.

Nevertheless, all plots show that the ICON model successfully reproduced the ice cloud at the upper height levels as seen in the observation data. The drizzle at lower height levels, however, is shown by 1–2 km higher and does reappear at later hours, in contrast to observation.

Simulation values of Z_h, V_D and SW_tot result in a higher overall range. For Z_h values differ by a factor of 0.25–0.33 (< 1 since values are on the negative scale). V_D values differ by a factor of around 1.67 and SW_tot values by a factor of 2–8.

5 Conclusion

In the present study, two simulation outputs from the ICON modelling framework were compared. Differing only in one key anthropogenic forcing, CCN, by a factor of 4, significant changes were detected and attributed. Polarimetric radar variables differential reflectivity Z_{DR} and specific differential phase K_{DP} were analyzed. Subsequently the simulation output was compared with observational data from the HOPE project. Hereby an attempt at attributing an anthropogenic effect to CCN concentration was made. The radar variables horizontal reflectivity Z_h, radial velocity V_D and total spectrum width SW_tot were analyzed.

In the comparison of simulations, differences appear to be significant for Z_{DR}. The 4xCCN simulation produces particles of more oblate shape at 3 km height, being slightly shifted to the west in contrast to a region of oblate particles at 5 km height in the 1xCCN simulation. In heights of up to 5 km, Z_{DR} values of cloud elements are higher in the 4xCCN simulation, indicating particles that are more oblate and greater in size. Above 5 km height levels, the 4xCCN particles are less oblate and smaller in size.

The differences are less significant for K_{DP}. In comparison to the 1xCCN simulation, the case of a fourfold CCN value simulation produces a cloud of slightly higher number concentration.

It has to be noted that especially the latter result may be seen out of appropriate geographical context. For instance, it is possible that the 4xCCN simulation produces approximately the same values as the 1xCCN simulation, but shifted horizontally.

In the comparison of simulation with observation, ICON shows similar patterns to measurements. The upper height pattern appears at comparable height levels, while the lower height pattern appears around 1 km higher. The values are higher in the simulation, by factors of 1.67–8.

The 4xCCN simulation seems to be slightly closer to observation. This would invalidate the ICON model capacities.

However, because of the comparably low temporal resolution of 15 min in the simulation and because of an estimation made about the selected area, this result is strongly speculative and not to be considered valid.

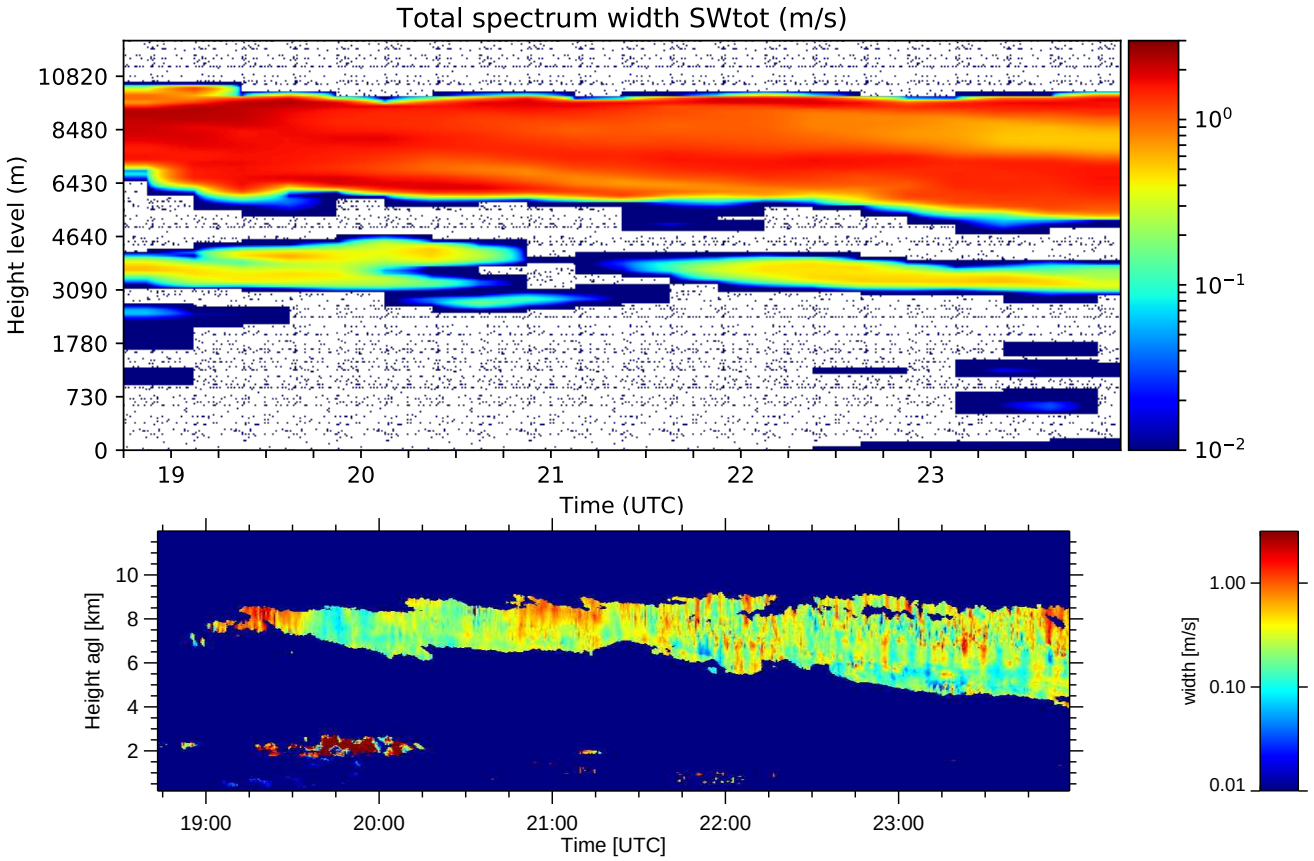

Figure 5: SW_{tot} for Krauthausen, above: ICON-Simulation, 4xCCN; below: HOPE-Observation

Overall it became clear that CCN concentrations affect clouds and precipitation. To attribute the effect to anthropogenic influence, however, the change must be detected for the 4xCCN simulation run. This means, in a comparison with observation, the 4xCCN run must show to be of greater difference than the 1xCCN run to the observation. As this attribution was not possible due to poor comparability in the comparison, it is only possible to conclude that CCN is weather relevant.

In further research studies, higher temporal resolutions should be implemented, as the ICON model provides a temporal resolution of 10 s (Zängl et al. [2015]). With such a resolution, a valid comparison of simulation and observation, and furthermore an attribution of anthropogenic influence to aerosol concentration would be feasible. The exact area where the observation data is valid should also be determined.

These further studies may expand over any time frame within April and May 2013 where observational data from the HOPE project is available.

Comparing ICON simulation data in terms of polarimetric variables would be useful as well, for more possibilities of comparison. To that end, observation of HOPE supersites that deployed the X-band radar network would be necessary (Zängl et al. [2015]). Further studies could also include other polarimetric variables, such as the co-polar correlation coefficient that, to date, is not being outputted by CR-SIM.

References

R. J. Doviak and D. S. Zrnic. Doppler radar and weather observations. *Academic Press, Second Addition*, 2006.

A. Gassmann and H.-J. Herzog. Towards a consistent numerical compressible non-hydrostatic model using generalized Hamiltonian tools. *Q. J. R. Meteorol. Soc*, 134:1597–1613, 2008. doi: 10.1002/qj.297.

R. Heinze, A. Dipankar, C. Henken Carbajal, C. Moseley, O. Sourdeval, S. Trömel, X. Xie,

P. Adamidis, F. Ament, H. Baars, C. Barthlott, A. Behrendt, U. Blahak, S. Bley, S. Brdar, M. Brueck, S. Crewell, H. Deneke, P. Di Girolamo, R. Evaristo, J. Fischer, C. Frank, P. Friederichs, T. Göcke, K. Gorges, L. Hande, M. Hanke, A. Hansen, H.-C. Hege, C. Hoose, T. Jahns, N. Kalthoff, D. Klocke, S. Kneifel, P. Knippertz, A. Kuhn, T. van Laar, A. Macke, V. Maurer, B. Mayer, C.I. Meyer, S.K. Muppa, R.A.J. Neggers, E. Orlandi, F. Pantillon, B. Pospichal, N. Röber, L. Scheck, A. Seifert, P. Seifert, F. Senf, P. Siligam, C. Simmer, S. Steinke, B. Stevens, K. Wapler, M. Weniger, V. Wulfmeyer, G. Zängl, D. Zhang, and J. Quaas. Large-eddy simulations over Germany using ICON: A comprehensive evaluation. *Q. J. R. Meteorol. Soc*, 143:69–100, 2017. doi: 10.1002/qj.2947.

IPCC. Third Assessment Report. The Scientific Basis, 6.7.8 Discussion of Uncertainties, 2001a. URL `https://web.archive.org/web/20020228024246/http://www.grida.no/climate/ipcc_tar/wg1/237.htm#678`.

IPCC. Third Assessment Report. The Scientific Basis, 7.2.2.5 Representation of cloud processes in models, 2001b. URL `http://ipcc.ch/ipccreports/tar/wg1/275.htm`.

IPCC. Climate Change 2007: Working Group I: The Physical Science Basis, 1.3.3 Detection and Attribution, 2007. URL `https://www.ipcc.ch/publications_and_data/ar4/wg1/en/ch1s1-3-3.html`.

IPCC. Climate Change 2013: The Physical Science Basis – Technical Summary, 2013. URL `https://www.ipcc.ch/pdf/assessment-report/ar5/wg1/WG1AR5_TS_FINAL.pdf`.

A. P. Khain, N. BenMoshe, and A. Pokrovsky. Factors Determining the Impact of Aerosols on Surface Precipitation From Clouds: An Attempt at Classification. *Journal of the Atmospheric Sciences*, 65:1721–1748, 2007. doi: 10.1175/2007JAS2515.1.

M. R. Kumjian. Principles and Applications of Dual-Polarization Weather Radar. Part I: Description of the Polarimetric Radar Variables. *J. Operational Meteor*, 1(19):226–242, 2013. doi: 10.15191/nwajom.2013.0121.

U. Lohmann and J. Feichter. Impact of sulfate aerosols on albedo and lifetime of clouds: A sensitivity study with the ECHAM4 GCM. *Journal of Geophysical Research*, 102:13685–13700, 1997. doi: 10.1029/97JD00631.

A. Macke, Baars H. Seifert, P., C. Beekmans, A. Behrendt, B. Bohn, B.L. Madhavan, B. Brügmann, E. Hammann, A. Hirsikko, J. Bühl, M. Cacciani, U. Corsmeier, S. Crewell, T. Damian, P. Di Girolamo, A. Graf, J. Handwerker, J. Kalisch, N. Kalthoff, S. Kinne, M. Kohler, H. Linné, U. Löhnert, S. Metzendorf, S.K. Muppa, M. Pfeiffer, B. Pospichal, C. Simmer, F. Späth, A. Riede, T. Ruhtz, D. Stelitano, A. Scaccione, I. Serikov, D. Summa, K. Träumner, A. Wieser, and V. Wulfmeyer. The HD(CP)^2 Observational Prototype Experiment (HOPE) – an overview. *Atmos. Chem. Phys*, 17:4887–4914, 2017. doi: 10.5194/acp-17-4887-2017.

H. Morrison, J. A. Curry, and V. I. Khvorostyanov. A new double-moment microphysics parameterization for application in cloud and climate models. Part I: Description. *J. Atmos. Sci*, 62:16651677, 2005.

H. Morrison, G. Thompson, and V. Tatarskii. Impact of cloud microphysics on the development of trailing stratiform precipitation in a simulated squall line: Comparison of one- and two-moment schemes. *Mon. Wea. Rev*, 137:991–1007, 2009.

A. Seifert and K. Beheng. A two-moment cloud microphysics parameterization for mixed-phase clouds. Part I: Model description. *Meteorol. Atmos. Phys*, 92:45–66, 2006. doi: 10.1007/s00703-005-0112-4.

A. Tatarevic and P. Kollias. User's Guide CR-SIM Software v 3.0. *Applied Radar Science Group*, 2017. URL `https://www.bnl.gov/CMAS/cr-sim.php`.

G. Thompson, P. R. Field, R. M. Rasmussen, and W. D. Hall. Explicit forecasts of winter precipitation using an improved bulk microphysics scheme. Part II: Implementation of a new snow

parameterization. *Mon. Wea. Rev*, 136:5095–5155, 2008.

TROPOS. Quicklook Archive of Cloudnet-processed data products of TROPOS, Krauthausen, 2018. URL http://lacros.rsd.tropos.de/cloudnet/cloudnet.php?site=krauthausen&year=2013&month=05&day=02&plot=1.

Wikipedia. Aerosol, 2018a. URL https://en.Wikipedia/wiki/Aerosol.

Wikipedia. Climate Change, 2018b. URL https://en.Wikipedia/wiki/Climate_change.

Wikipedia. dBZ (meteorology), 2018c. URL https://en.Wikipedia/wiki/DBZ_(meteorology).

Wikipedia. Inverse Problem, 2018d. URL https://en.Wikipedia/wiki/Inverse_problem.

Wikipedia. Millimeter Cloud Radar, 2018e. URL https://en.Wikipedia/wiki/Millimeter_cloud_radar.

Wikipedia. Global Warming, 2018f. URL https://en.Wikipedia/wiki/Global_warming.

R. Wolke, O. Knoth, O. K. Hellmuth, W. Schröder, and E. Renner. The parallel model system LM-MUSCAT for chemistry-transport simulations: Coupling scheme, parallelization and application. *Parallel Computing: Software Technology, Algorithms, Architectures, and Applications*, pages 363–370, 2004.

R. Wolke, W. Schröder, R. Schroedner, and E. Renner. Influence of grid resolution and meteorological forcing on simulated European air quality: A sensitivity study with the modeling system COSMO-MUSCAT. *Atmos. Environ*, 53:110–130, 2012. doi: 10.1016/j.atmosenv.2012.02.085.

G. Zängl, D. Reinert, P. Rípodas, and M. Baldauf. The ICON (ICOsahedral Non-hydrostatic) modelling framework of DWD and MPI-M: Description of the non-hydrostatic dynamical core. *Q. J. R. Meteorol. Soc*, 141:563–579, 2015. doi: 10.1002/qj.2378.